ACS OMEGA

http://pubs.acs.org/journal/acsodf

Article

Understanding Ash Sintering Variation Behaviors of Low-Rank Coals with Municipal Sludge Addition Based on Mineral Interactions

Fenghai Li,* Ziqiang Yang, Yong Wang, Guangheng Liu, Meiling Xu, Hongli Fan, Wei Zhao, Chaoyue Zhao, Tao Wang, and Yitian Fang

Cite This: *ACS Omega* 2022, 7, 10588−10598

Read Online

ACCESS | Metrics & More | Article Recommendations

ABSTRACT: Co-gasification with coal provides an economically viable way to use sludge. To investigate the effect of municipal sludge (MS) on the sintering behaviors of low-rank coals (LRCs) and their modification mechanisms, the initial sintering temperature (T_s) of three LRCs and their mixtures with MS addition were tested by a T_s analyzer, an X-ray diffractometer, and FactSage calculation. The results show that the T_s values of Xiaolongtan coal (XLT), Xiangyuan coal (XY), and Daliuta coal (DLT) all increase with MS addition. The 9−12% MS mass ratio is suitable during LRC fluidized-bed gasification to mitigate ash-related issues. The T_s is closely related to the liquid-phase content or the transmissions of microparticles (e.g., atoms and ions) or blank spots during heating, while the ash fusion temperatures (AFTs) are mainly determined by acid/base ratios. The T_s values of high-Fe XLT and XY mixed ashes increased gradually with increasing MS proportion because the sintering mechanisms transferred from liquid phase to solid phase, while for relatively high-Mg DLT ashes, the T_s values increased with increasing MS proportions, which might result from the formations of high-melting-point minerals (e.g., $Ca_3(PO_4)_2$ and Mg_2SiO_4). The results deepen the understanding of ash sintering behaviors and provide references to alleviate ash-related issues during gasification.

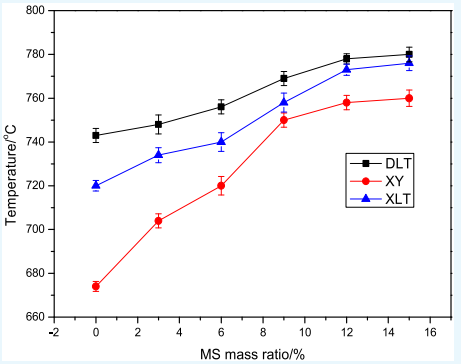

1. INTRODUCTION

Increasing attention has been paid to biomass globally due to environmental pressure, because it is carbon-neutral, renewable, abundant, and widely distributed.[1,2] In China, to achieve carbon peaks by 2030 and carbon neutrality by 2060, it is necessary to increase the percentage of biomass energy.[3] Among the main biomass types—agriculture and its residues, forestry and its residues, livestock manures, and sewage sludge—the amount of sewage sludge has accumulated recently due to urbanization and industrialization.[4,5] For example, the municipal sludge (MS) in China is predicted to exceed 60 million tons by 2020,[6] with 21 million tons textile dyeing sludge produced annually.[7] The huge amounts of sludge impose tremendous strain on environment pollution and do great harm to humans. Thus, it is of importance to utilize sludge properly for environmental protection and conservation of natural resources.

Methods for the disposal of sludge generally include landfills, composting, and thermal conversion.[8] Landfills occupy huge amounts of land and are liable to cause secondary pollution,[9] while composting takes a long time, pollutes the air (through the emissions of odors and bioaerosols), and may contaminate soil and underground water.[10] The sludge contains low amounts of fixed carbon and high levels of volatile matter and can be used as an alternative fuel.[5] Thermal conversion has been considered as an effective sludge disposal method to decrease waste, recover energy, and eliminate pathogenic bacteria.[11] Among the sludge thermal conversion technologies (e.g., pyrolysis, gasification, and combustion), gasification is regarded as an effective way for synthetic natural gas, chemical products (ammonia, lipid compounds, and hydrogen olefin), liquid fuels (gasoline, diesel, and methanol), and power generation.[12,13] However, the negative characteristics of sludge, such as low calorific value and high ash and moisture contents, severely limit its monogasification. Thus, the co-gasification with coal provides an economically viable way for its clean disposal.

Low-rank coal (LRC), accounting for about 50% of global coal reserves,[14] plays an important role in chemical products and energy markets.[15] Compared with other coals, the lower combustion efficiency of LRC and its higher emissions of carbon (due to its high contents of moisture, volatile matter, and oxygen) limit its direct combustion in power plants.

Received: January 8, 2022
Accepted: February 25, 2022
Published: March 15, 2022

Table 1. Proximate and Ultimate Analyses of the Samples[a]

	proximate analysis/(wt%)				ultimate analysis/(wt%)				
sample	M_{ad}	V_{ad}	A_{ad}	FC_{ad}[b]	C_{ad}	H_{ad}	O_{ad}[b]	N_{ad}	$S_{t,ad}$
DLT	8.17	28.21	5.31	58.31	60.59	4.42	20.44	0.80	0.27
XY	11.04	35.88	9.47	43.61	56.53	3.60	17.15	1.12	1.09
XLT	10.05	28.26	13.38	48.31	54.66	3.28	17.57	0.47	0.59
MS	15.36	36.61	38.47	9.56	30.26	1.26	11.94	1.55	1.06

[a]Abbreviations: ad, air-dried basis; t, total; M, moisture; V, volatile matter; A, ash; FC, fixed carbon. [b]By difference.

Gasification, potentially dealing with CO_2 release, on a commercial scale is regarded as an effective conversion technology to utilize the LRC due to its high reaction activity.[16−18] Considering the advantages of fluidized-bed gasification (feedstock flexibility (e.g., biomass, coal, de-oiled asphalt, petroleum coke, manure,[19,20] and sewage sludge[21]), uniform bed temperature, low cost, good gas−solid contact condition,[22] easy scale-up,[23] and environmental friendliness) and the high reactivity of LRC and sewage sludge, it may be a suitable option. However, problems related to ash (e.g., agglomeration, de-fluidization, deposition, and slag formation) are generally found in fluidized-bed gasification processes.[24]

Although ash fusion temperatures (AFTs) are generally used to provide references for reactor design and operation parameter selection, the reproducibility of AFT results may be a major problem due to its geometric variation criteria explicitly ignoring shrinkage.[25] The ash fusion process can be divided into three stages: sintering, primary fusion, and free liquid.[26] Sintering is one of the dominant factors of the above problems during fluidized-bed conversion, and it provides a way to understand the mechanisms of ash deposition, fouling, and slagging during the conversions of carbonaceous materials.[27,28] Therefore, it is necessary to explore the ash sintering characteristics to develop their co-gasification technology.

Sintering is the process of particle softening and surface flow under the driving force of reduction of free surface energy, which leads particles to adhere together.[24] Sintering behavior is mainly determined by the ash's chemical composition[29] and affected by atmosphere and pressure.[24] The sintering characteristics are closely related to alkali-metal content (especially for Na[30]). Fan et al. found that the sintering temperatures (T_s) of Jincheng or Jiaozuo coal ashes decreased continuously with increasing percent of peanut shell ash (PHA), which resulted from the generation of low-melting-point (MP) potassium silicates (PHA < 20%), the fusion of sylvite, and the formations of adularia, potassium sulfide, and diopside (PHA ranges from 30% to 50%).[31] Mitigation of the sintering degree of cotton stalk was ascribed to a decrease in KCl content with increasing high silicon−aluminum content coal ash (e.g., Shajuzi coal and Pingshuo coal).[32] Tabakaev et al. pointed out that the suitable amount of peat addition to bran during co-combustion of peat and bran was 5 wt%, and a decrease in the peat proportion caused ash residue sintering.[33] Haykiri-Acma et al. found that hazelnut shell addition made the T_s and deformation temperature (DT) of lignite increase due to its relatively high CaO content, while the rice husk showed a limited effect on the T_s of lignite.[34] Zhou et al. investigated the effects of biomass on sintering characteristics of bituminous coal ash and found that a high proportion of wood pellets inhibited low-MP Shenhua sintering but promoted high-MP Shanxi coal sintering, while a high blend ratio of corn stalk ash promoted the sintering of both coals.[35] Luan et al. indicated that the coal ash T_s decreased with increasing biomass percentage.[36] Zhang et al. pointed out that lignite ash T_s increased with increasing ashing temperature but decreased with increasing K_2CO_3 percentage, and when the ashes were prepared at the same temperature, the T_s was the highest for ash with rich alumina content.[37] Namkung et al. reported that the degree of sintering of herbaceous biomass ash increased with increasing time, while it was alleviated obviously by alkali-metal leaching, which further significantly mitigated the ash adhesion and corrosion behaviors.[38] Meng et al. found that the T_s of Qinghai coal ash decreased from 1005 °C to 855, 834, and 819 °C with the addition of 30−50% of Laoheishan, Fushun, and Xinghua oil shales, respectively.[39]

The ash sintering characteristics of the blends vary with different fuels and ash formation conditions, and the ash sintering behaviors of the blends cannot be predicted directly according to the individual fuel characteristics because of the differences in their ash composition and reaction complexity;[35] thus, the various sintering mechanisms are not clarified and require further exploration. Moreover, MS generally contains relatively high phosphorus and low silicon compared with coal.[21] To our limited knowledge, the investigations concerning the effects of MS on sintering behaviors are relatively few. Thus, the objectives of this paper were to investigate the sintering properties of three LRCs and their T_s variation behaviors with MS addition under a reducing atmosphere, and to explore their modification mechanisms from a mineral transformation perspective. The results deepen the understanding of sintering behaviors and provide some references to alleviate ash-related issues during the co-gasification of LRC and sludge in fluidized bed.

2. RESULTS AND DISCUSSION

2.1. Sintering and Fusion Characteristics of Raw Materials. Four air-dried raw samples were selected in this experiment. The three LRCs, namely Daliuta coal (DLT, from Inner Mongolia Autonomous Region), Xiangyang coal (XY, from Hubei Province), and Xiaolongtan coal (XLT, from Hunan Province), were provided by a pilot plant for pulverized coal gasification engineering, Institute of Coal Chemistry, Chinese Academy of Sciences. The air-dried MS was obtained from a municipal wastewater treatment plant (Heze, Shandong Province) through air flotation, hydrolysis acidification, anaerobic contact oxidation, de-coloration, sedimentation, and dehydration, which has been described in detail in a previous paper.[5] The four samples were ground to a size <200 μm. Proximate analyses were performed on a 5E-MAC III infrared fast coal analyzer (Kaiyuan, Co. Ltd. Changsha, China) according to methods GB/T212-2008 and GB/T28731-2012 for coal and biomass, respectively, and the ultimate analyses of the four materials using a 2400 II elemental analyzer (PerkinElmer, Waltham, USA) are shown

https://doi.org/10.1021/acsomega.1c07138
ACS Omega 2022, 7, 10588−10598

in Table 1. The contents of ash and volatile matter of MS were obviously higher than those of the three LRCs, respectively, while the fixed carbon content of MS was obviously lower than those of the three LRCs.

The sintering and fusion characteristics were studied on a sintering tester and AFT analyzer, respectively. The results are shown in Table 2. The T_s increased in the sequence of XY < XLT < DLT < MS, which was almost the same order as that of AFTs. A good correlation was found between the T_s of coal ashes and its basicity values (B, bases = K_2O + Na_2O + CaO + MgO + Fe_2O_3).[24] The metal cations in the basic compositions destroyed the silica chain, making a bridging oxide bond change into a non-bridging oxide bond,[40] which might lead to a decrease in its T_s. The ash compositions tested on an XRF spectrometer (XRF-1800, Shimadzu, Japan) are presented in Table 3. The B values of four samples were calculated and are shown in Table 3. The B values decrease in the order XY > XLT > DLT > MS, which might explain the differences in ash sintering and fusion characteristics of the four samples.

Moreover, under a reducing atmosphere, the T_s is closely related to the total contents of Na_2O, Fe_2O_3, and SO_3,[14] because under a reducing atmosphere their interactions might result in the formations of a Na_2S-FeS (MP = 640 °C) eutectic,[24] which was proven in XRD measurements of the ash samples (see Figure 4). The total content of Na_2O, Fe_2O_3, and SO_3 in four samples decreased in the sequence of XY (27.03%) > XLT (17.03%) > MS (15.33%) > DLT (7.31%) (Table 3). This explained the T_s differences for XY, XLT, and DLT. The iron can easily form glassy state substances and cause ash sintering.[41] The calcium and iron accelerated the reaction with aluminosilicate to form the eutectic and made T_s and AFT decrease.[42] The total contents of CaO and Fe_2O_3 in ash samples were XY (48.57%), XLT (33.76%), MS (26.08%), and DLT (24.36%), which resulted in the differences in AFTs for XY, XLT, and DLT. The MS with high T_s and AFT might have a high phosphorus content (P_2O_5: 20.30%), which might react with calcium and potassium and form high-MP phosphates (e.g., $Ca(PO_3)_2$, $K_2CaP_2O_7$, and $Ca_2P_2O_7$).[43]

Table 2. Sintering and Fusion Temperatures of Raw Material Ashes[a]

		AFT (°C)			
sample	T_s (°C)	DT	ST	HT	FT
DLT	743	1117	1179	1210	1230
XY	674	1064	1127	1143	1183
XLT	720	1098	1156	1167	1191
MS	791	1128	1186	1208	1245

[a]Abbreviations: T_s, sintering temperature; DT, deformation temperature; ST, softening temperature; HT, hemispheric temperature; FT, flow temperature.

2.2. The Effects of MS on the Sintering and Fusion Characteristics of LRCs. The T_s values of the three mixed LRCs with MS addition are shown in Figure 1. The T_s values of XLT, XY, and DLT all increased with the addition of MS ash. The trends in the variation of T_s of XLT and DLT with MS ash addition were almost the same: they both increased slowly (0−12%) and then changed not obviously; the T_s of XY increased quickly (0−12%), and then slowly (10−12%), and then not obviously. The increasing T_s decreased the risk of the adhesion and deposition on the heating surface,[35] the fouling on the syngas cooler, and metal corrosion in the gasifier.[29]

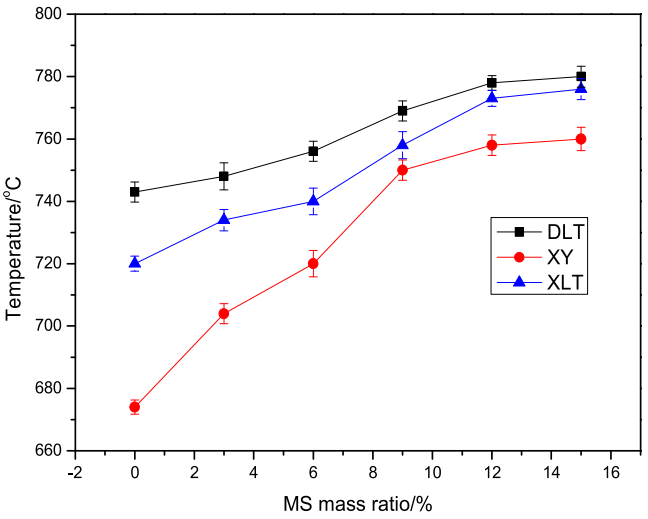

Figure 1. Variations in the T_s values of the three LRCs with MS addition.

Among the four characteristic temperatures of ashes, DT is a relatively more important parameter to guide reactor design and determine the operating conditions because the DT change is more sensitive to the ash composition variation than are ST, HT, and FT.[44] As shown in Figure 2, the AFT variations for three coals were different with increasing MS mass ratio: Taking DT for example, the mixed AFTs for DLT or XLT increased slowly, while the XY-mixed AFTs showed a little decrease with the increasing mass ratio of MS. High DT decreased the occurrence potential for silicate-melt-induced slagging during fluidized-bed gasification.[45] Thus, to abate the slagging formation on the heating surface of the gasifier, it is generally required that the operating temperature is 50−100 °C lower than its DT. In industrial practice, the operating temperature of fluidized-bed gasification generally ranges from 850 to 950 °C. Therefore, the DT is generally required to be not less than 1050 °C from the perspective of AFT. MS addition is an effective way to mitigate ash-related issues with DLT and XLT during gasification. As for XY, the MS addition is controversial; the suitable MS mass ratio is not more than

Table 3. Ash Compositions of Raw Materials

	ash composition (%)											
sample	B	Na_2O	K_2O	MgO	CaO	SO_3	Fe_2O_3	Al_2O_3	SiO_2	Cl_2O	TiO_2	P_2O_5
DLT	35.02	0.69	0.75	9.22	18.46	0.66	5.90	21.57	42.14	–	0.52	0.09
XY	53.73	0.20	2.08	2.88	24.61	0.99	23.96	13.32	31.06	–	0.74	0.16
XLT	36.28	0.82	1.04	0.66	19.86	2.14	13.90	19.44	41.51	–	0.48	0.15
MS	32.99	0.21	5.38	1.32	14.28	0.15	11.80	16.58	29.71	0.27	–	20.3

https://doi.org/10.1021/acsomega.1c07138
ACS Omega 2022, 7, 10588−10598

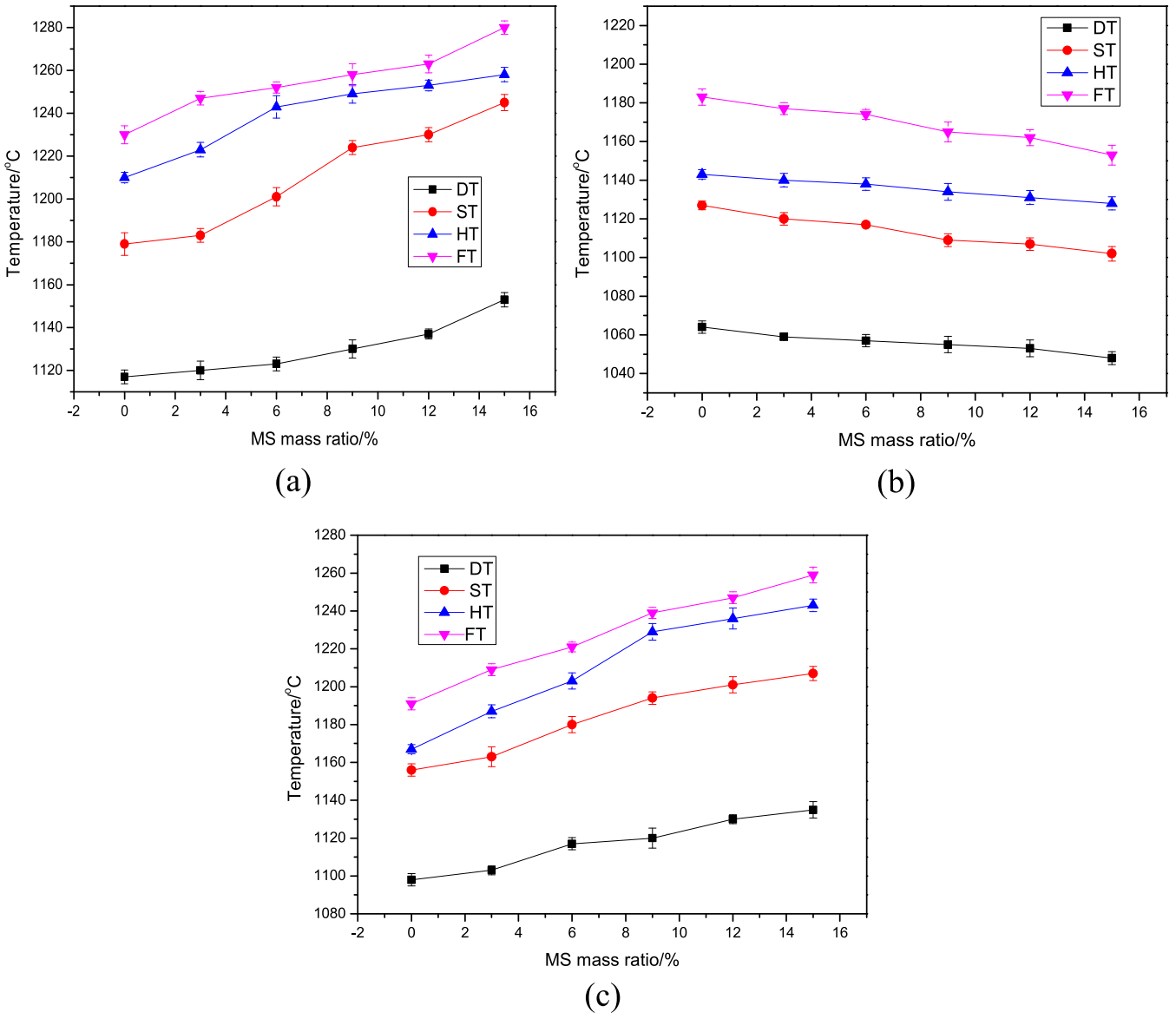

Figure 2. AFT variation of three mixtures with increasing MS mass ratio: (a) DLT, (b) XY, and (c) XLT.

12%. In industrial practice, the additive mass ratio (accounting for the percent of the total mass) is generally less than 10%;[46] thus, the suitable mass ratio for MS addition may be 9−12% to mitigate ash-related issues during LRC fluidized-bed gasification.

The ash composition of mixtures and their acid/base mass ratio (A/B) values (based on Table 2) are presented in Table 4. With MS addition, the A/B values in three kinds of mixed ashes all increased gradually. In a certain temperature range, the higher the A/B value of coal ashes, the higher is the T_s.[26] Moreover, the B values of three mixed ashes with MS addition decreased correspondingly, and T_s generally decreased with the B values;[24] this explains the increases in the T_s with increasing MS mass ratio. The T_s of XY increased relatively obviously with MS addition, which might be related to its high contents of CaO and Fe_2O_3 (24.61% + 23.96% = 48.57%), which were prone to form their eutectics, and made the XY T_s low.

The variation in their AFTs with increasing MS mass ratio maybe explained in this way. The ash samples can be considered as tetrahedral silicate networks at high temperature.[47] The A/B ratio is a more accurate parameter to explain their fusion characteristics from the perspective of network theory. The AFTs are the lowest when the A/B value is around 1; the more the A/B value deviates from 1, the higher the AFTs are.[12,48] The A/B values of XY mixtures gradually reach 1 (0.86 → 0.98) with increasing MS mass ratio, which might result in the AFTs of the mixtures decreasing. In contrast, for DLT and XLT mixtures, the A/B values deviated from 1 further for DLT with MS addition than for XLT. This explains the differences in AFT variation for three coal ashes with MS addition.

2.3. Investigation on T_s Variation Mechanisms of LRCs with Increasing MS Mass Ratio. *2.3.1. XRD Analyses of Three Coal Laboratory Ash Samples and Their Sintered Ashes.* During heating, the interactions of minerals in the ash samples resulted in the variations in mineral components and their content. Thus, it is necessary to measure the mineral composition of ash samples at the T_s to investigate the T_s variation mechanism. Figure 3 shows the XRD patterns of 575 °C laboratory ashes and sintered ashes of three LRCs. The

https://doi.org/10.1021/acsomega.1c07138
ACS Omega 2022, 7, 10588−10598

Table 4. Ash Compositions of Mixed Ash Samples

	ash composition (%)											
sample	A/B^a	Na_2O	K_2O	MgO	CaO	SO_3	Fe_2O_3	Al_2O_3	SiO_2	Cl_2O	TiO_2	P_2O_5
DLT	1.85	0.69	0.75	9.22	18.46	0.66	5.90	21.57	42.14	–	0.52	0.09
+3% MS	1.86	0.68	0.89	8.98	18.33	0.64	6.08	21.42	41.77	0.01	0.51	0.69
+6% MS	1.86	0.66	1.03	8.75	18.21	0.63	6.25	21.27	41.39	0.02	0.49	1.30
+9% MS	1.87	0.65	1.17	8.51	18.08	0.61	6.43	21.12	41.02	0.03	0.47	1.91
+12%MS	1.88	0.63	1.31	8.28	17.95	0.60	6.61	20.97	40.64	0.03	0.46	2.52
+15%MS	1.89	0.62	1.44	8.04	17.83	0.58	6.79	20.82	40.28	0.04	0.44	3.12
XY	0.86	0.20	2.08	2.88	24.61	0.99	23.96	13.32	31.06	–	0.74	0.16
+3% MS	0.88	0.20	2.18	2.83	24.30	0.96	23.60	13.42	31.02	0.01	0.72	0.76
+6% MS	0.91	0.20	2.28	2.79	23.99	0.94	23.23	13.52	30.98	0.01	0.7	1.36
+9% MS	0.93	0.20	2.38	2.74	23.68	0.91	22.87	13.61	30.94	0.02	0.68	1.97
+12%MS	0.95	0.20	2.48	2.69	23.37	0.89	22.50	13.71	30.90	0.03	0.65	2.58
+15%MS	0.98	0.20	2.58	2.65	23.06	0.86	22.14	13.81	30.86	0.04	0.62	3.18
XLT	1.75	0.82	1.04	0.66	19.86	2.14	13.90	19.44	41.51	–	0.48	0.15
+3% MS	1.76	0.80	1.17	0.68	19.69	2.08	13.84	19.35	41.16	0.01	0.47	0.75
+6% MS	1.77	0.78	1.30	0.70	19.53	2.02	13.77	19.27	40.80	0.02	0.45	1.36
+9% MS	1.78	0.76	1.43	0.72	19.36	1.96	13.71	19.18	40.45	0.02	0.44	1.97
+12%MS	1.79	0.75	1.56	0.74	19.19	1.90	13.65	19.10	40.09	0.03	0.42	2.57
+15%MS	1.80	0.73	1.69	0.76	19.02	1.84	13.59	19.01	39.73	0.04	0.42	3.17

[a]Acid/base mass ratio.

crystalline compounds of XLT ash prepared at 575 °C were mostly composed of quartz (SiO_2), anhydrite ($CaSO_4$), illite ($KAl_2(OH)_2AlSi_3O_{10}$), calcite ($CaCO_3$), oldhamite (CaS), pyrite (FeS_2), and sodium sulfide (Na_2S). Pyrrhotite ($Fe_{1-x}S$), sulfide (Na_2FeS_2), and pyroxferroite ($(Fe_{0.86}Ca_{0.14})SiO_3$) were generated in the sintered XLT ashes. As for XY ash samples, although there was a difference in the mineral content between the laboratory ashes of XY and XLT, the kinds of minerals in the XY laboratory ashes were the same as in XLT. Greigite (Fe_3S_4) was found in XY sintered ashes with a relatively high content of iron (Fe_2O_3, 23.96%) compared with that of XLT. Pyrrhotite ($Fe_{1-x}S$) was produced from the reduction of pyrite.[49] The low-temperature eutectic sulfides (e.g., Na_2S–FeS) resulted from the interactions of Fe_2O_3, Na_2O, and SO_3;[24] the interactions of FeO, CaO, and SiO_2 resulted in the formation of pyroxferroite. Moreover, the mixtures of illite in the presence of pyrite and calcite formed a molten solution at 600–650 °C.[50] Thus, the interaction of minerals led to the formations of partial-melting phases on the surface of the ash particles. Then, under the force of free surface energy reduction, the partial-melting phase flowed to the interface between adjacent ash particles, causing the adhesion of ash particles, and gradually resulted in formation of large ash aggregates. Simultaneously, the closed pores among ash particles became smaller and the open pores grew larger, and gases traveled through the open pores and caused the pressure drop. The temperature corresponding to pressure drop was the T_s of ash.

As shown in Figure 3, quartz, anhydrite, illite, calcite, pyrite, sodium sulfide (Na_2S), and dolomite ($CaMg(CO_3)_2$) were found in the DLT laboratory ashes; pyroxferroite and anorthite ($CaAlSi_2O_8$) were generated in the DLT sintered ashes. Sintering in a reducing atmosphere occurred due to the formation of Ca or Fe silicates. The generation of anorthite resulted from the reaction between Ca-containing mineral (e.g., anhydrite) and metakaolin. (The obvious protrusion baseline between 20° 2θ and 30° 2θ indicated the existence of the amorphous structure of highly reactive metakaolin,[51] which was derived from the transformation of illite or kaolinite.) Moreover, during heating, the anhydrate decomposed into lime, which reacted with quartz and ferrous oxide to form pyroxferroite (pyroxferroite and anorthite), as indicated by its crystallization during cool-down (see Figure 4c).[52] These generations of relatively large molecular silicates might cause the small molecular cramming, which leads to the ability to form sintering bridges between the fine ash particles and to an increase in the compression strength of ash samples.[28,53] Thus, the sintering of DLT ash might be connected with solid-phase sintering.

2.3.2. T_s Variation Mechanisms of Coal Ash with Increasing MS Mass Ratio. The XRD patterns of sintered ash samples of XLT, XY, and DLT with different MS ash mass ratios are presented in Figures 4, 5, and 6, respectively. As for the three LRC ashes and their mixtures, with increasing temperature, the illite undergoes dehydroxylation at 450–550 °C, and then might react with partially oxidized pyrite and calcium oxide (derived from the decomposition of anhydrite and calcite) to generate silicate glass and then formed a liquid phase at 750 °C.[54] As can be seen from the three figures, with increasing MS proportion, the content of sulfides (e.g., sulfide (Na_2FeS_2), pyrrhotite ($Fe_{1-x}S$), or gregite (Fe_3S_4); the sintering on reducing atmosphere was initiated by ferrous sulfide melting[52]) with low MP gradually decreased and disappeared, while the silicates with relatively high MP formed in the corresponding sintered ash samples and their content increased gradually. For XLT mixed ash, the newly formed phases were mainly in the form of calcium silicates ($Ca_3Fe_2Si_3O_4$, $CaAl_2Si_2O_8$, and $CaFeSiO_4$) due to its relatively high content of calcium and silicon, while in the sintered XY mixed ash samples, ferrous salts (e.g., $FeAl_2O_4$, $Ca_2FeSi_2O_7$, $CaFeSiO_4$, and $CaFeSi_2O_6$) and potassium salt (e.g., $KAlSi_2O_6$) formed due to its relatively high iron content (>20.00%); relatively high-MP magnesium silicates (Mg_2SiO_4, MP = 1910 °C; $CaMgSiO_4$, MP = 1390 °C) were found in the DLT mixed

https://doi.org/10.1021/acsomega.1c07138
ACS Omega 2022, 7, 10588–10598

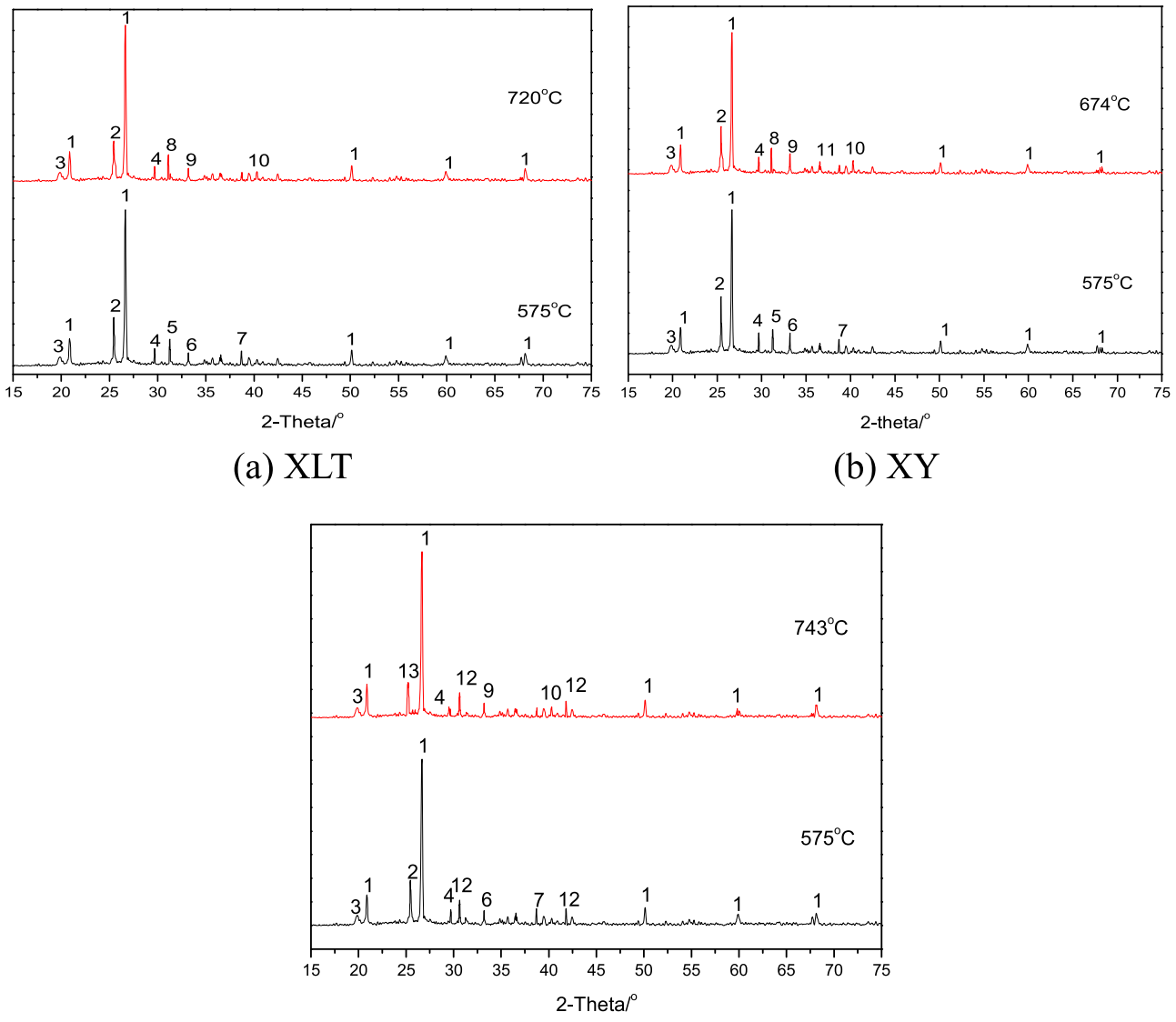

Figure 3. XRD patterns of three laboratory and sintered ashes: (a) XLT, (b) XY, and (c) DLT. Peak labels: 1, quartz (SiO_2); 2, anhydrite ($CaSO_4$); 3, illite ($KAl_2(OH)_2AlSi_3O_{10}$); 4, calcite ($CaCO_3$); 5, oldhamite (CaS); 6, pyrite (FeS_2); 7, sodium sulfide (Na_2S); 8, sulfide (Na_2FeS_2); 9, pyroxferroite ($(Fe_{0.86}Ca_{0.14})SiO_3$); 10, pyrrhotite ($Fe_{1-x}S$); 11, greigite ($Fe_3S_4$); 12, dolomite ($CaMg(CO_3)_2$); and 13, anorthite ($CaAlSi_2O_8$).

sintered ash samples. Moreover, the high-MP whitlochite ($Ca_3(PO_4)_2$, MP = 1391 °C) was found in mixed sintered ash samples with increasing MS ash mass ratio due to its relatively high P content (P_2O_5, 20.30%). The ionic potential of P^{5+} (147 nm^{-1}) is higher than that of Si^{4+} (95 nm^{-1}),[12] which results in its higher tendency to react with calcium than that of Si^{4+}. It might be deduced that the following reactions occurred during heating:[12,14,24,27]

$$\text{calcite } (CaCO_3) \rightarrow \text{lime } (CaO) + CO_2 \quad (1)$$

$$\text{anhydrite } (CaSO_4) \rightarrow \text{lime } (CaO) + CO_2 \quad (2)$$

$$\text{dolomite } (Ca(Mg)CO_3) \rightarrow \text{lime } (CaO) \text{ or magnesia } (MgO) + CO_2 \quad (3)$$

$$\text{lime } (CaO) + \text{magnesia } (MgO) + \text{quartz } (SiO_2) \rightarrow \text{monticellite } (CaMgSiO_4) \quad (4)$$

$$\text{pyrrhotite } (Fe_{1-x}S) + H_2 \text{ or CO} \rightarrow \text{wustite } (FeO) + \text{other sulfides} \quad (5)$$

$$\text{wustite } (FeO) + \text{alumina } (Al_2O_3) \rightarrow \text{hercynite } (FeAl_2O_4) \quad (6)$$

$$\text{lime } (CaO) + \text{wustite } (FeO) + \text{quartz } (SiO_2) \rightarrow \text{kirscheteite } (CaFeSiO_4) \quad (7)$$

$$\text{kirscheteite } (CaFeSiO_4) + \text{quartz } (SiO_2) \rightarrow \text{hedenbergite } (CaFeSi_2O_6) \quad (8)$$

https://doi.org/10.1021/acsomega.1c07138
ACS Omega 2022, 7, 10588−10598

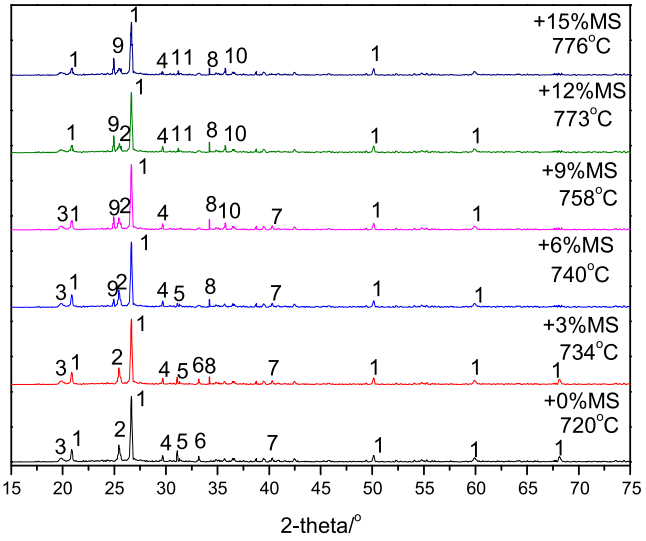

Figure 4. XRD patterns of sintered ash samples of XLT with different MS mass ratios. Peak labels: 1, quartz (SiO_2); 2, anhydrite ($CaSO_4$); 3, illite ($KAl_2(OH)_2AlSi_3O_{10}$); 4, calcite ($CaCO_3$); 5, sulfide (Na_2FeS_2); 6, pyroxferroite ($(Fe_{0.86}Ca_{0.14})SiO_3$); 7, pyrrhotite ($Fe_{1-x}S$); 8, andradite ($Ca_3Fe_2Si_3O_{11}$); 9, anorthite ($CaAl_2Si_2O_8$); 10, whitlochite ($Ca_3(PO_4)_2$); and 11, kirscheteite ($CaFeSiO_4$)

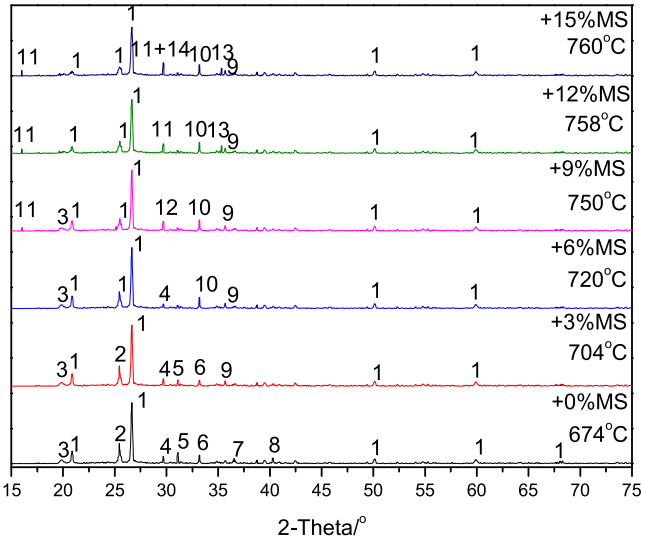

Figure 5. XRD patterns of sintered ash samples of XY with different MS mass ratios. Peak labels: 1, quartz (SiO_2); 2, anhydrite ($CaSO_4$); 3, illite ($KAl_2(OH)_2AlSi_3O_{10}$); 4, calcite ($CaCO_3$); 5, sulfide (Na_2FeS_2); 6, pyroxferroite ($(Fe_{0.86}Ca_{0.14})SiO_3$); 7, gregite ($Fe_3S_4$); 8, pyrrhotite ($Fe_{1-x}S$); 9, hercynite ($FeAl_2O_4$); 10, ferroakermanite ($Ca_2FeSi_2O_7$); 11, lecuite ($KAlSi_2O_6$); 12, kirschstennite ($CaFeSiO_4$); 13, whitlochite ($Ca_3(PO_4)_2$); and 14, hedenbergite ($CaFeSi_2O_6$).

$$\text{hedenbergite } (CaFeSi_2O_6) + \text{lime } (CaO) \rightarrow \text{ferroakermanite } (Ca_2FeSi_2O_7) \quad (9)$$

$$\text{ferroakermanite } (Ca_2FeSi_2O_7) + \text{kirscheteite } (CaFeSiO_4) \rightarrow \text{andradite } (Ca_3Fe_2Si_3O_{11}) \quad (10)$$

$$3\ \text{calcium oxide } (CaO) + \text{phosphorus pentoxide } (P_2O_5) \rightarrow \text{whitlochite } (Ca_3(PO_4)_2) \quad (11)$$

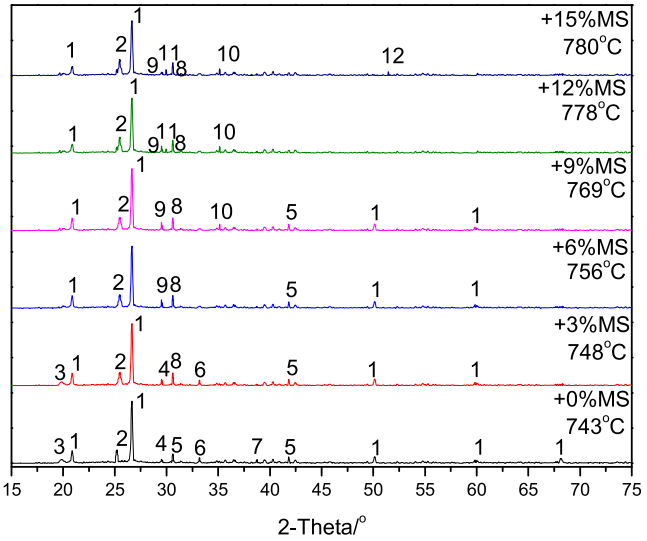

Figure 6. XRD patterns of sintered ash samples of DLT with different MS mass ratios. Peak labels: 1, quartz (SiO_2); 2, anorthite ($CaAl_2Si_2O_8$); 3, illite ($KAl_2(OH)_2AlSi_3O_{10}$); 4, calcite ($CaCO_3$); 5, dolomite ($CaMg(CO_3)_2$); 6, pyroxferroite ($(Fe_{0.86}Ca_{0.14})SiO_3$); 7, pyrrhotite ($Fe_{1-x}S$); 8, clinopyroxene ($CaMgSi_2O_6$); 9, hedenbergite ($CaFeSi_2O_6$); 10, whitlochite ($Ca_3(PO_4)_2$); 11, forsterite ($Mg_2SiO_4$); and 12, monticellite ($CaMgSiO_4$).

$$\text{anorthite } (CaAl_2Si_2O_8) + \text{quartz } (SiO_2) + \text{potassium oxide } (K_2O) \rightarrow \text{lime } (CaO) + \text{orchoclase } (KAlSi_3O_8) \quad (12)$$

$$\text{orchoclase } (KAlSi_3O_8) \rightarrow \text{lecuite } (KAlSi_2O_6) + \text{quartz } (SiO_2) \quad (13)$$

2.4. Variation Analyses of Liquid-Phase Content by FactSage Calculation. The sintering process is closely related to the formation of the liquid phase and its content. The proportions of solid and liquid phases in ash samples with increasing temperature can be predicated by FactSage calculation.[55,56] Based on a material-transfer process, coal ash sintering is mainly divided into liquid-phase sintering and solid-phase sintering. For liquid-phase sintering, some liquid phase appeared during liquid-phase sintering. The powder particles were gradually extruded due to the different surface states of ash powder particles and capillary pressures, which resulted in the diffusion of particles with large surface curvature in the liquid-phase substances. After liquid-phase diffusion, the particles precipitated on the neck surface with large curvature, concave or powder contact; it was called the "dissolution precipitation" process. In contrast, in solid-phase sintering, the microparticles (atoms, ions, etc.) or blank spots (vacancies) in ash powder particles transferred materials by means of surface diffusion, interface diffusion, or internal diffusion with increasing temperature (i.e., "diffusion mass transfer" process).

Considering the ranges of T_s and AFTs of mixed samples (T_s = 650−800 °C, FT < 1300 °C), the calculations were carried out from 600 to 1300 °C with an interval of 30 °C under the conditions of reducing atmosphere and atmospheric pressure (0.1 MPa). The results are shown in Figure 7. It can be seen clearly that, although the liquid-phase variations for XY or XLT mixtures with MS addition were different under high temperatures (>950 °C), the liquid phase was generated for

https://doi.org/10.1021/acsomega.1c07138
ACS Omega 2022, 7, 10588−10598

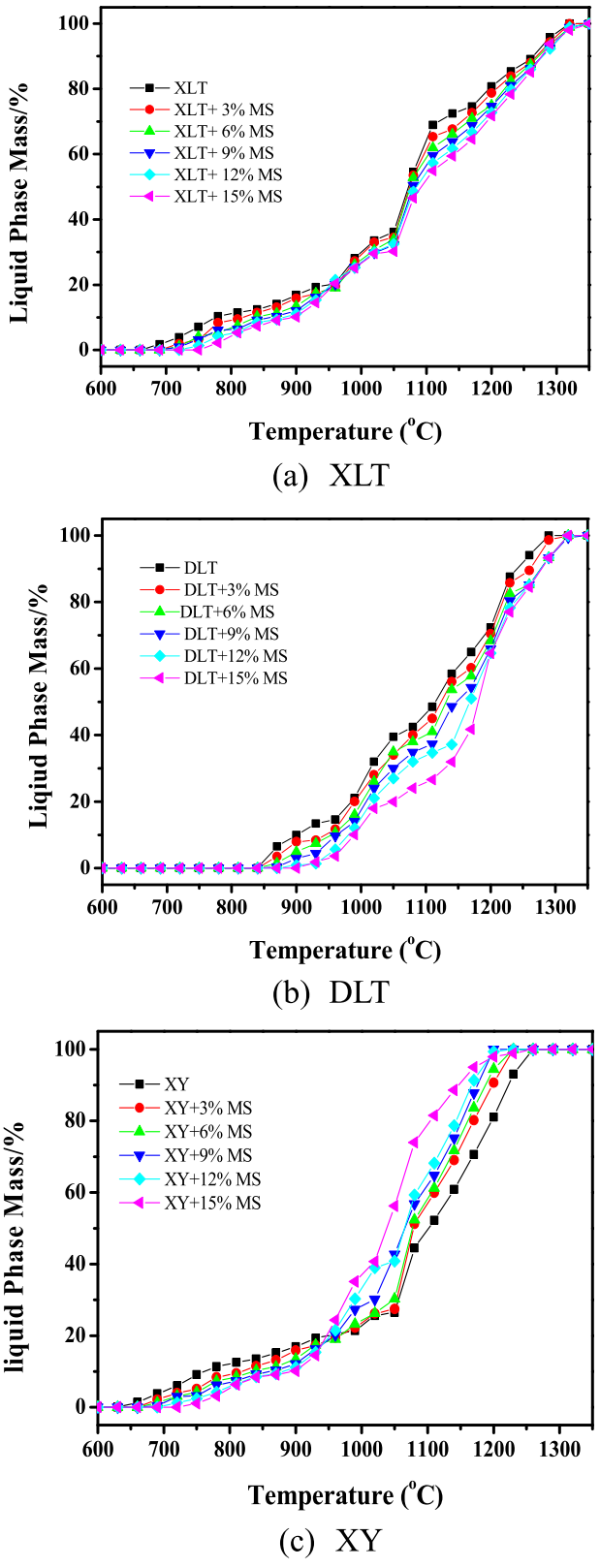

Figure 7. Liquid-phase content of mixed ashes with increasing temperature: (a) XLT, (b) DLT, and (c) XY.

both XY and XLT and their mixtures, and their liquid-phase content gradually decreased with increasing MS proportion below their T_s (800 °C). The low-MP sulfides (e.g., Na_2FeS_2, $Fe_{1-x}S$, and greigite Fe_3S_4) in their sintered ash samples (Figures 4 and 5) might result from the precipitation of their liquid phase. Moreover, the formation of relatively high-MP minerals with increasing MS mass ratio might result in the liquid-phase contents decreasing gradually (<800 °C) in sintered ash samples. With the liquid-phase content decreased, the sintering mechanisms might transfer to solid-phase sintering (diffusion mass-transfer process).

As for DLT ash samples and its mixtures, liquid-phase mineral content was not found when the temperature was less than its T_s (Figure 6), consistent with Figure 8 (low-MP sulfide was not found in its sintered samples). This indicates that the sintering might result from the diffusion of microparticles or blank spots (solid-phase diffusion). It was also found by Schimpoke et al. that mineral transitions were responsible for the initial sintering for high silicon−aluminum coal.[47] The increases in T_s with increasing MS ash mass ratio might result from the formations of relatively high-MP minerals (e.g., $Ca_3(PO_4)_2$ and Mg_2SiO_4).

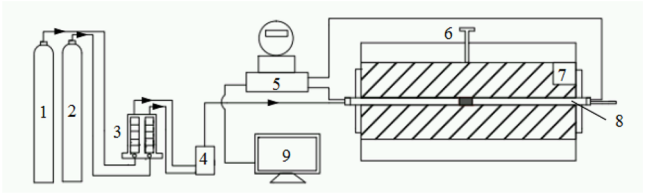

Figure 8. Schematic diagram of PDT 500 sintering furnace: 1, CO_2 cylinder; 2, H_2 cylinder; 3, flow controller; 4, gas mixing tank; 5, differential pressure transmitter; 6, thermocouple; 7, heater; 8, mullite tube; and 9, computer.

Furthermore, it can be shown that, at the same temperature, the liquid contents of XLT and DLT mixtures generally increased with increasing MS proportions, while for XY mixtures, its liquid-phase content first decreased (below 950 °C) and then increased. This could explain why the AFTs decreased with increasing MS mass ratio for XY mixtures.

3. CONCLUSIONS

(1) The T_s values increased in the sequence of XY< XLT < DLT < MS. The T_s values of XLT, XY, and DLT all increased with MS addition. A 9−12% MS mass ratio might be suitable to mitigate the ash-related issues during LRC fluidized-bed gasification.

(2) The T_s is mostly related to the liquid-phase content or the transmissions of microparticles or blank spots under relatively low temperatures, while the AFT is mainly determined by the A/B.

(3) The T_s modification mechanisms are different with variation of ash composition. For XLT and XY mixed ashes, the T_s increased with increasing MS due to the sintering mechanism transformation from liquid phase to solid phase. The T_s increases for high-Mg DLT with MS addition resulted from the formations of high-MP minerals (e.g., $Ca_3(PO_4)_2$ and Mg_2SiO_4).

4. EXPERIMENTAL SECTION

4.1. Ash Preparation. The volatility of the alkaline elements (Na and K) was <8% during ashing temperatures in 500−600 °C;[57] the volatility of relatively low alkaline element contents in raw materials could be neglected below 600 °C.[1] The laboratory ashes of the three LRCs, MS, and

https://doi.org/10.1021/acsomega.1c07138
ACS Omega 2022, 7, 10588−10598

their mixtures (MS proportions of 3, 6, 9, 12, and 15% were mixed with each of the three LRCs) were prepared based on ASTM E1755-01 standards. The samples were placed in an SX2-8-16ASP muffle furnace (Kewei Co., Beijing, China), which first was increased to 250 °C at 10 °C/min and maintained at that temperature for 30 min. After that, the temperature was increased to 575 °C within 30 min and was kept for 3 h. Finally, the ashes were taken out, cooled to room temperature, and kept in a drying oven before analyses.

4.2. Measurement of Ash T_s and Its Sintered Ash Samples. The T_s was measured by a pressure-drop method, which was sensitive and repeatable.[58,59] The sintering experiment was tested on a PDT 500 sintering furnace (Tairui Ltd. Co., Xuzhou, China), the schematic diagram of which is presented in Figure 8. About 0.5 g of ash sample was put into a mullite tube with an inner diameter of 7.5 mm and pressed for 10 min under 30 MPa to make an ash pellet. The mullite tube with ash pellet was placed into the sintering furnace. Before heating, the air in the mullite tube was replaced by reducing gas (1:1 H_2/CO_2, volume ratio) at 6 mL·min^{-1} for 30 min. The T_s was tested at the conditions of 3 mL·min^{-1} and 5 °C·min^{-1}, respectively. During measurement, the curve of pressure difference with increasing temperature was obtained, in which the temperature corresponding to the pressure-difference turning point was the T_s.[24] The sintered ash pellet was cooled to room temperature, taken out from the mullite tube, crushed to <0.074 mm, and stored in a desiccator before analyses.

4.3. AFT Measurement. An ALHR-2 AFT tester (Aolian, Chanzhou, China) was used to determine the AFTs in reducing atmosphere (1:1 H_2/CO_2, volume ratio) according to ASTM D1857 procedure. The triangular pyramidal ash cone was transferred into the tester and heated at 15 °C·min^{-1} up to 900 °C and 5 °C·min^{-1} after 900 °C until it fused completely or reached the maximum temperature of the AFT (1500 °C). The four characteristic temperatures, namely deformation temperature (DT), softening temperature (ST), hemispheric temperature (HT), and flow temperature (FT), were determined based on the variations in ash cone shape during the fusion process.

4.4. Analytical Method. The ash compositions were tested on an X-ray fluorescence (XRF) spectrometer (XRF-1800, Shimadzu, Japan). A D/max-rB X-ray diffractometer (XRD, Rigaku Co., Tokyo, Japan) with Cu Kα radiation under the conditions of 40 kV and 100 mA was used to measure the mineral compositions of ash samples. The samples were scanned from 15° 2θ to 70° 2θ at 5° 2θ·min^{-1} scanning speed.

4.5. Thermodynamic Calculations. The main ash compositions (SiO_2, Al_2O_3, K_2O, CaO, MgO, Fe_2O_3, SO_3, Na_2O, and P_2O_5) were selected for thermodynamic calculations to predict liquid-phase content with increasing different temperatures by using the Equilib module of FactSage 7.3. The calculations were carried out from 600 to 1000 °C with an interval of 30 °C under reducing atmosphere (1:1 H_2/CO_2, volume ratio).

AUTHOR INFORMATION

Corresponding Author

Fenghai Li − *School of Chemistry and Chemical Engineering, Heze University, Heze, Shandong 274015, China; School of Chemistry and Chemical Engineering, Henan Polytechnic University, Jiaozuo, Henan 454003, China; Shandong Hongda Chemical Co., Ltd, Heze, Shandong 274700, China;* orcid.org/0000-0003-1690-3346; Email: qflfh74@126.com

Authors

Ziqiang Yang − *School of Chemistry and Chemical Engineering, Henan Polytechnic University, Jiaozuo, Henan 454003, China*

Yong Wang − *Shandong Hongda Chemical Co., Ltd, Heze, Shandong 274700, China*

Guangheng Liu − *Shandong Hongda Chemical Co., Ltd, Heze, Shandong 274700, China*

Meiling Xu − *School of Chemistry and Chemical Engineering, Heze University, Heze, Shandong 274015, China*

Hongli Fan − *School of Chemistry and Chemical Engineering, Heze University, Heze, Shandong 274015, China*

Wei Zhao − *School of Chemistry and Chemical Engineering, Henan Polytechnic University, Jiaozuo, Henan 454003, China*

Chaoyue Zhao − *School of Chemistry and Chemical Engineering, Henan Polytechnic University, Jiaozuo, Henan 454003, China*

Tao Wang − *School of Chemistry and Chemical Engineering, Heze University, Heze, Shandong 274015, China*

Yitian Fang − *State Key Laboratory of Coal Conversion, Institute of Coal Chemistry, Chinese Academy of Sciences, Taiyuan, Shanxi 030001, China*

Complete contact information is available at: https://pubs.acs.org/10.1021/acsomega.1c07138

Notes

The authors declare no competing financial interest.

ACKNOWLEDGMENTS

This work was financially supported by National Natural Science Foundations of China (21875059) and the Natural Science Foundation of Shandong Province, China (ZR2018MB037, ZR2021MB011).

REFERENCES

(1) Li, F.; Yu, B.; Li, J.; Wang, Z.; Guo, M.; Fan, H.; Wang, T.; Fang, Y. Exploration of potassium migration behavior in straw ashes under reducing atmosphere and its modification by additives. *Renew. Energy* **2020**, *145*, 2286−2295.

(2) Lv, Y.; Niu, Y.; Liang, Y.; Liu, S.; Wang, D.; Hui, S. Experiment and kinetics studies on ash fusion characteristics of biomass/coal mixtures during combustion. *Energy Fuels* **2019**, *33*, 10317−10323.

(3) Yishui, T.; Ming, S.; Geng, K.; Linwei, M.; Si, S. Development strategy of biomass economy in China. *Chin. J. Eng. Sci.* **2021**, *23*, 133−140.

(4) Pio, D. T.; Tarelho, L. A. C.; Nunes, T. F. V.; Baptista, M. F.; Matos, M. A. A. Co-combustion of residual forest biomass and sludge in a pilot-scale bubbling fluidized-bed. *J. Clean Prod.* **2020**, *249*, 119309.

(5) Li, F.; Zhao, W.; Fan, H.; Xu, M.; Lu, J.; Zhao, C.; Guo, M.; Guo, Q.; Fang, Y. Effects of sludge on the ash fusion behaviors of corn stalk and its modification mechanisms. *Fuel* **2021**, *293*, 120378.

(6) Wang, T.; Hou, H.; Ye, Y.; Rong, H.; Li, J.; Xue, Y. Combustion behavior of refuse-derived fuel produced from sewage sludge and rice husk/wood sawdust using thermogravimetric and mass spectrometric analyses. *J. Clean Prod.* **2019**, *222*, 1−11.

(7) Liu, Y.; Ran, C.; Siyal, A. A.; Song, Y.; Jiang, Z.; Dai, J.; Chtaeva, P.; Fu, J.; Ao, W.; Deng, Z.; Zhang, T. Comparative study for fluidized bed pyrolysis of textile dyeing sludge and municipal sewage sludge. *J. Hazard. Mater.* **2020**, *396*, 122619.

(8) Yu, G.; Chen, D.; Arena, U.; Huang, Z.; Dai, X. Reforming sewage sludge pyrolysis volatile with Fe-embedded char: minimization of liquid product yield. *Waste Manage.* **2018**, *73*, 464−475.
(9) Yan, M.; Feng, H.; Zheng, R.; Yu, C.; Hantoko, D.; Zhou, Z.; Zhang, Y.; Kanchanatip, E. Sulfur conversion and distribution during supercritical water gasification of sewage sludge. *J. Energy Instit* **2021**, *95*, 61−68.
(10) Lin, M.; Ning, X.; Liang, X.; Wei, P.; Wang, Y.; Liu, J. Study of the heavy metals residual in the incineration slag of textile dyeing sludge. *J. Taiwan Inst Chem. Eng.* **2014**, *45*, 1814−1820.
(11) Xie, W.; Wen, S.; Liu, J.; Xie, W.; Kuo, J.; Lu, X.; Sun, S.; Chang, K.; Buyukada, M.; Evrendilek, F. Comparative thermogravimetric analyses of co-combustion of textile dyeing sludge and sugarcane bagasse in carbon dioxide/oxygen and nitrogen/oxygen atmospheres: Thermal conversion characteristics, kinetics, and thermodynamics. *Bioresour. Technol.* **2018**, *255*, 88−95.
(12) Li, F.; Fan, H.; Wang, X.; Wang, T.; Fang, Y. Influences of phosphorus on ash fusion characteristics of coal and its regulation mechanism. *Fuel* **2019**, *239*, 1338−1350.
(13) Kokalj, F.; Arbiter, B.; Samec, N. Sewage sludge gasification as an alternative energy storage model. *Energy Convers. Manage.* **2017**, *149*, 738−747.
(14) Li, F.; Zhao, C.; Guo, Q.; Li, Y.; Fan, H.; Guo, M.; Wu, L.; Huang, J.; Fang, Y. Exploration in ash-deposition (AD) behavior modification of low-rank coal by manure addition. *Energy* **2020**, *208*, 118293.
(15) Lu, G.; Bai, Y.; Lv, P.; Wang, J.; Song, X.; Su, W.; Yu, G. Insights into the role of calcium during coal gasification in the presence of silicon and aluminum. *Fuel* **2021**, *302*, 121134.
(16) Ma, M.; Wang, J.; Bai, Y.; Lv, P.; Song, X.; Su, W.; Ding, L.; Wei, J.; Yu, G. Deactivation mechanism of coal char gasification reactivity induced by cow manure biomass volatile-coal char interactions. *Fuel* **2021**, *301*, 121064.
(17) Xie, L.; Xu, L.; Ma, X. Influence of the Direct Coal Liquefaction Residue on the Fusion Characteristics of Jincheng Coal with a High Ash Fusion Temperature. *Energy Fuels* **2020**, *34*, 1355−1364.
(18) Li, H.; Kong, L.; Bai, J.; Bai, Z.; Guo, Z.; Li, W. Modification of ash flow properties of coal rich in calcium and iron by coal gangue addition. *Chin J. Chem. Eng.* **2021**, *35*, 239−246.
(19) Li, F.; Li, Y.; Zhao, C.; Fan, H.; Xu, M.; Guo, Q.; Guo, M.; Wang, Z.; Huang, J.; Fang, Y. Investigation on ash-fusion characteristics of livestock manure and low-rank coals. *Energy Fuels* **2020**, *34*, 5804−5812.
(20) Ma, M.; Bai, Y.; Wang, J.; Lv, P.; Song, X.; Su, W.; Yu, G. Study on the pyrolysis characteristics and kinetic mechanism of cow manure under different leaching solvents pretreatment. *J. Environ. Manage.* **2021**, *290*, 112580.
(21) Liu, H.; Zhang, S.; Feng, S.; Liu, J.; Liu, G.; Sun, B.; Che, D.; Wang, Q. Influence of sewage sludge on ash fusion during combustion of maize straw. *Energy Fuels* **2019**, *33*, 10237−10246.
(22) Li, X.; Zhi, L.; Shi, W.; Kong, L.; Bai, J.; Yu, J.; Reinmoller, M.; Guhl, S.; Meyer, B.; Li, W. Effect of K_2O/Na_2O on fusion behavior of coal ash with high silicon and aluminum level. *Fuel* **2020**, *265*, 116964.
(23) Barisano, D.; Canneto, G.; Nanna, F.; Alvino, E.; Pinto, G.; Villone, A.; Carnevale, M.; Valerio, V.; Battafarano, A.; Braccio, G. Steam/oxygen biomass gasification at pilot scale in an internally circulating bubbling fluidized-bed reactor. *Fuel Process. Technol.* **2016**, *141*, 74−81.
(24) Ji, S.; Li, F.; Wang, T.; Li, Z.; Fang, H.; Huang, J.; Fang, Y. Investigation on the sintering behaviors of low-temperature lignite ashes. *J. Therm. Anal. Calorim.* **2014**, *117*, 1311−1320.
(25) Hsieh, P. Y. Sintering and collapse of synthetic coal ash and slag cones as observed through constant heating rate optical dilatometry. *Fuel* **2019**, *235*, 567−576.
(26) Zhang, L.; Wang, J.; Wei, J.; Bai, Y.; Song, X.; Xu, G.; Pan, Y.; Yu, G. Synergistic effects of CaO and MgO on ash fusion characteristics in entrained-flow gasifier. *Energy Fuels* **2021**, *35*, 425−432.
(27) Yao, X.; Zheng, Y.; Zhou, H.; Xu, K.; Xu, Q.; Li, L. Effects of biomass blending, ashing temperature and potassium addition on ash sintering behaviour during co-firing of pine sawdust with a Chinese anthracite. *Renew. Energy* **2020**, *147*, 2309−2320.
(28) Zhou, H.; Luo, J.; Wang, Z.; Ji, M.; Zhang, M. Effect of walnut shell ash on pore structure characteristics during Zhundong coal sintering. *Fuel Process. Technol.* **2021**, *221*, 106923.
(29) Shi, W.; Laabs, M.; Reinmoller, M.; Bai, J.; Guhl, S.; Kong, L.; Li, H.; Meyer, B.; Li, W. In-situ analysis of the effect of CaO/Fe_2O_3 addition on ash melting and sintering behavior for slagging-type applications. *Fuel* **2021**, *285*, 119090.
(30) Wang, W.; Xu, Z.; Wei, B.; Zhang, L.; Tan, H.; Yang, T.; Mikulcic, H.; Duic, N. The ash deposition mechanism in boilers burning Zhundong coal with high contents of sodium and calcium: A study from ash evaporating to condensing. *Appl. Therm. Eng.* **2015**, *80*, 150−159.
(31) Fan, H.; Li, F.; Guo, Q.; Guo, M. Effect of biomass ash on initial sintering and fusion characteristics of high melting coal ash. *J. Energy Instit.* **2021**, *94*, 129−138.
(32) Fan, H.; Li, F.; Guo, Q.; Guo, M. Effect of high silicon-aluminum coal ashes on sintering and fusion characteristics of a potassium-rich biomass ash. *J. Energy Instit.* **2020**, *93*, 1781−1789.
(33) Tabakaev, R.; Ibraeva, K.; Kan, V.; Dubinin, Y.; Rudmin, M.; Yazykov, N.; Zavorin, A. The effect of co-combustion of waste from flour milling and highly mineralized peat on sintering of the ash residue. *Energy* **2020**, *196*, 117157.
(34) Haykiri-Acma, H.; Yaman, S.; Kucukbayrak, S. Effect of biomass on temperatures of sintering and initial deformation of lignite ash. *Fuel* **2010**, *89*, 3063−3068.
(35) Zhou, H.; Luo, Z.; Liu, D.; Ma, M. Effect of biomass ashes on sintering characteristics of high/low melting bituminous coal ash. *Fuel Process. Technol.* **2019**, *189*, 62−73.
(36) Luan, C.; You, C.; Zhang, D. Composition and sintering characteristics of ashes from co-firing of coal and biomass in a laboratory-scale drop tube furnace. *Energy* **2014**, *69*, 562−570.
(37) Zhang, J.; Li, J.; Zhu, M.; Zhang, Z.; Zhou, B.; Shen, G.; Zhang, D. A phenomenological investigation into potassium migration and ash sintering characteristics during p.f. combustion of lignites with and without K_2CO_3 addition. *Appl. Therm. Eng.* **2019**, *148*, 64−77.
(38) Namkung, H.; Lee, Y.-J.; Park, J.-H.; Song, G. S.; Choi, J. W.; Kim, J.-G.; Park, S.-J.; Park, J. C.; Kim, H.-T.; Choi, Y.-C. Influence of herbaceous biomass ash pre-treated by alkali metal leaching on the agglomeration/sintering and corrosion behaviors. *Energy* **2019**, *187*, 115950.
(39) Meng, Y.; Jiang, P.; Yan, Y.; Pan, Y.; Wu, X.; Zhao, H.; Sharmin, N.; Lester, E.; Wu, T.; Pang, C. An advanced ash fusion study on the melting behaviour of coal, oil shale and blends under gasification conditions using picture analysis and graphing method. *Chin. J. Chem. Eng.* **2021**, *32*, 393−407.
(40) Wu, C.; Wang, B.; Zheng, J.; Li, H. Flux mechanism of compound flux on ash and slag of coal with high ash melting temperature. *Chin. J. Chem. Eng.* **2019**, *27*, 1200−1206.
(41) Mao, Y.; Jin, Y.; Li, K.; Bi, J.; Li, J.; Xin, F. Sintering behavior of different coal ashes in catalytic coal gasification process. *J. Fuel Chem. Technol.* **2015**, *43*, 402−409.
(42) Zhu, Y.; Liu, Y.; Wang, L.; Yang, W.; Yang, H.; Jiang, L.; Du, Z.; Shao, J.; Chen, H. Effect of phosphorus-based additives on the sintering characteristics of cornstalk ash. *J. Energy Instit.* **2021**, *97*, 37−47.
(43) Li, F.; Wang, X.; Zhao, C.; Li, Y.; Guo, M.; Fan, H.; Guo, Q.; Fang, Y. Influence of additives on potassium retention behaviors during straw combustion: A mechanism study. *Bioresour. Technol.* **2020**, *299*, 122515.
(44) Li, F.; Li, Y.; Fan, H.; Wang, T.; Guo, M.; Fang, Y. Investigation on fusion characteristics of deposition from biomass vibrating grate furnace combustion and its modification. *Energy* **2019**, *174*, 724−734.
(45) Niu, Y.; Tan, H.; Hui, S. Ash-related issues during biomass combustion: alkaliinduced slagging, silicate melt-induced slagging

https://doi.org/10.1021/acsomega.1c07138
ACS Omega 2022, 7, 10588−10598

(ash fusion), agglomeration, corrosion, ash utilization, and related countermeasures. *Prog. Energy Combust. Sci.* **2016**, *52*, 1−61.
(46) Li, F.; Zhao, C.; Li, J.; Li, Y.; Zhao, H.; Fan, H.; Xu, M.; Wang, Z.; Huang, J.; Fang, Y. Investigation on ash fusion behavior modification of wheat straw by sludge addition. *J. Energy Instit.* **2021**, *98*, 1−10.
(47) Schimpke, R.; Klinger, M.; Krzack, S.; Meyer, B. Determination of the initial ash sintering temperature by cold compression strength tests with regard to mineral transitions. *Fuel* **2017**, *194*, 157−165.
(48) Howaniec, N.; Smoliński, A. Influence of fuel blend ash components on steam co-gasification of coal and biomass chemometric study. *Energy* **2014**, *78*, 814−825.
(49) Li, F.; Huang, J.; Fang, Y.; Wang, Y. The effects of leaching and floatation on the ash fusion temperatures of three selected lignites. *Fuel* **2011**, *90*, 2377−2383.
(50) Matjie, R. H.; Li, Z. S.; Ward, C. R.; French, D. Chemical composition of glass and crystalline phase in coarse coal gasification ash. *Fuel* **2008**, *87*, 857−869.
(51) Wan, Q.; Rao, F.; Song, S. Reexamining calcination of kaolinite for the synthesis of metakaolin geopolymers-roles of dehydroxylation and recrystallization. *J. Non-Cryst. Solids* **2017**, *460*, 74−80.
(52) Schimpke, R.; Klinger, M.; Krzack, S.; Meyer, B. Determination of the initial ash sintering temperature by cold compression strength tests with regard to mineral transitions. *Fuel* **2017**, *194*, 157−165.
(53) Wang, F.; Yao, M.; Kan, H.; Kuang, J.; Li, P.; Zhang, J.; Zhang, Y. Effect of Al_2O_3/CaO on the melting and mineral transformation of Ningdong coal ash. *Chin. J. Chem. Eng.* **2020**, *28*, 3110−3116.
(54) Li, F.; Huang, J.; Fang, Y.; Wang, Y. Formation mechanism of slag during fluid-bed gasification of lignite. *Energy Fuels* **2011**, *25*, 273−280.
(55) Kong, L.; Bai, J.; Li, W.; Wen, X.; Li, X.; Bai, Z.; Guo, Z.; Li, H. The internal and external factor on coal ash slag viscosityat high temperatures, Part 3: Effect of CaO on the pattern of viscosity temperature curves of slag. *Fuel* **2016**, *179*, 10−16.
(56) Li, F.; Fan, H.; Guo, M.; Guo, Q.; Fang, Y. Influencing mechanism of additives on ash fusion behaviors of straw. *Energy Fuels* **2018**, *32*, 3272−3280.
(57) Huang, Y.; Liu, H.; Yuan, H.; Zhuang, X.; Yuan, S.; Yin, X.; Wu, C. Release and transformation pathways of various K species during thermal conversion of agricultural straw. Part 1: devolatilization stage. *Energy Fuels* **2018**, *32*, 9605−9613.
(58) Jing, N.; Wang, Q.; Luo, Z.; Cen, K. Effect of different reaction atmospheres on the sintering temperature of Jincheng coal ash under pressurized conditions. *Fuel* **2011**, *90*, 2645−2651.
(59) Jing, N.; Zhu, M.; Shen, G.; Wang, Q.; Zhang, D. Effect of ash preparation method on the sintering characteristics of ashes from combustion of coal and biomass blends. *Fuel* **2016**, *186*, 830−837.

https://doi.org/10.1021/acsomega.1c07138
ACS Omega 2022, 7, 10588−10598